Ion energy distribution in an electron beam ion trap inferred from simulations of the trapped ion cloud

Michael Hahn [*]

Columbia Astrophysics Laboratory, Columbia University, 550 West 120th Street, New York, New York 10027, USA

Thusitha Arthanayaka

Skidmore College, 815 North Broadway, Saratoga Springs, New York 12866, USA

Peter Beiersdorfer

Space Sciences Laboratory, University of California, Berkeley, California 94720, USA

Gregory V. Brown

Lawrence Livermore National Laboratory, Livermore, California 94550, USA

Daniel W. Savin

Columbia Astrophysics Laboratory, Columbia University, 550 West 120th Street, New York, New York 10027, USA

We have inferred the energy distribution of trapped ions in an electron beam ion trap (EBIT) from simulations of the spatial distribution of Fe^{13+} ions and a comparison with measured visible light images of the ion cloud. We simulated the cloud of Fe^{13+} ions by computing ion trajectories in the EBIT for different ion energy distributions used to initialize the trajectories. We then performed a least-squares fit to infer the ion energy distribution that best reproduced the measured ion cloud. These best-fit distributions were typically non-Maxwellian. For electron beam energies of 395–475 eV and electron beam currents of 1–9 mA, we find that the average ion energy is in the range of 10–300 eV. We also find that the average ion energy increases with increasing beam current approximately as $\langle E \rangle \approx 25 I_e$ eV, where I_e is the electron beam current in mA. We have also compared our results to Maxwell-Boltzmann-distribution ion clouds. We find that our best-fit non-thermal distributions have an $\langle E \rangle$ that is less than half that of the T from the best-fit Maxwell-Boltzmann distributions $(\langle E \rangle / q)/T = 0.41 \pm 0.05$.

I. INTRODUCTION

Electron beam ion traps (EBITs) are versatile sources for benchmarking fundamental atomic physics parameters as well as spectral fitting packages used to help interpret data measured from a variety of complex plasmas [1,2]. These traps have a cylindrical geometry with an electron beam running along the axis of the trap. Ions are confined radially within the trap by the electrostatic potential of the electron beam and by an applied axial magnetic field. Axial confinement is achieved by electrodes at the ends of the trapping region [3,4]. Trapped ions travel along trajectories that pass through the electron beam, but also extend out to larger radii. Collectively, these orbits form a cloud of trapped ions. The statistical distribution of the total ion energy is generally not well known in EBITs. As the total energy of each ion determines each individual trajectory, the energy distribution among all the ions determines the shape of the ion cloud.

The ion energy distribution is often assumed to be close to Maxwell-Boltzmann and characterized by an ion temperature T_i. (Throughout, temperatures are in energy units.) Because EBITs rely on electrostatic trapping, T_i is important for trapping and producing highly charged ions in the device. Lower T_i leads to narrower linewidths for precision spectroscopy [5–7]. Ion temperature is also important when an EBIT is used as an ion source [8–10]. For many applications, it is also useful to have experimental control over the ion energy. For example, some EBIT experiments seek to maximize the time that the ions spend within the electron beam. However, collisions between the electron beam and the ions increase the energy of the ions, mainly in the transverse direction [11]. This drives ion orbits to larger radii until they hit the inner wall of the trap and are lost. One approach to reducing the energy of the ions is sympathetic evaporative cooling. For this, a second, lower atomic number ion species is introduced into the trap. Ion-ion collisions between the high mass, highly charged species of interest and the low mass, lower charged second species transfer energy to the lighter ions. Since the lower charged ions are less strongly trapped electrostatically, they escape more easily, leaving behind less energetic higher mass ions [12]. Conversely, for other applications it can be beneficial to expand the ion orbits in order to dilute the effective electron density experienced by the ions [13–16]. In such

[*]mhahn@astro.columbia.edu

cases it would be desirable to increase the ion energy in order
to probe lower densities.

There have been several measurements of the ion temper-
ature in EBITs that have relied on measuring the Doppler
broadening of emission lines. For example, Beiersdorfer *et al.*
[17] measured the Doppler width for the x-ray $1s^2\,^2S_0 -$
$-1s2p\,^3P_2$ transition of Ti^{20+}. The inferred temperature for
Ti^{20+} was 550 eV, corresponding to about $27.5q$. Adler *et al.*
[18] inferred the ion temperature based on the width of a visi-
ble line of Ba^{34+} and obtained a temperature of $T_i \approx 500 -$
-1000 eV. Beiersdorfer *et al.* [19] measured the Doppler
width of the x-ray lines arising from the Cs^{45+} $(2p^5_{3/2}3d_{5/2})_{J=1}$
and $(2p^5_{1/2}3s_{1/2})_{J=1}$ upper levels to the $(2p^6)_{J=0}$ ground state.
They found a temperature below 60 eV due to efficient cool-
ing using Ne^{10+}. In another experiment, Beiersdorfer *et al.*
[20] performed similar measurements for Ti^{19+} using a high-
resolution crystal spectrometer and found temperatures in the
range of 70–700 eV, varying with the beam current.

All of these measurements have relied on inferring the
Doppler width of an observed spectral line, but for many
experiments, determining the ion temperature via Doppler
broadening is not practical. Hence, developing an alternative
method for determining the ion temperature is desirable. One
alternative is to use the spatial distribution of ions in the trap.
Because the potential of the trap varies radially, ions that are
more energetic will have a broader radial distribution. Porto
et al. [21] inferred T_i in an EBIT by considering the shape of
an ion cloud in thermal equilibrium produced by a Maxwell-
Boltzmann distribution of ions. However, Porto *et al.* [21]
point out that at high temperatures, where T_i is equal to the
potential at the edge of the electron beam, the ion clouds must
be nonthermal. Measurements based on Doppler broadening
also typically assume a Maxwellian line broadening. It would
be useful to have a diagnostic that can also characterize a
nonthermal ion energy distribution.

The method we introduce here is based on comparing test-
particle simulations of the ion orbits in EBIT to visible light
images of the ion cloud. We apply this method to ion cloud
images acquired during a recent set of experiments whose
objective was to calibrate electron-density-sensitive emission
lines in the extreme ultraviolet (EUV) [16]. The visible light
from the ions is due to a metastable level whose lifetime is or-
ders of magnitude longer than the orbital period of the trapped
ions. Consequently, the emission occurs throughout the ion
cloud and allows us to image the spatial distribution of the
ions. Arthanayaka *et al.* [16] measured the ion cloud in order
to determine the overlap between the ions and the electron
beam and the resulting effective electron density experienced
by the ions. Here, we use the Arthanayaka *et al.* measurements
to study the ion energy distribution. In their experiment, the
EUV spectra themselves could not be used to determine the
ion temperature because the spectral linewidths of the ob-
served allowed transitions were dominated by the width of the
electron beam. However, for a given ion energy distribution,
we can numerically follow a representative sample of particle
orbits and construct a synthetic ion cloud. The synthetic ion
cloud can then be compared to the observed ion cloud and
a least-squares fitting method used to iteratively vary the ion
energy distribution in the simulation until the measured and

synthetic ion clouds are in agreement. We used this method to
infer the ion energy distribution.

II. EXPERIMENT

Details of the ion cloud measurements using the EBIT-I
at the Lawrence Livermore National Laboratory have been
described in Refs. [16,22]. To review, the ions were confined
axially by a 400 V axial trapping potential created using a
set of three drift tubes. The radial confinement is due to the
radial electric field from the electron beam itself as well as
an applied axial magnetic field of 3 T. Iron pentacarbonyl
$Fe(CO)_5$ was injected into the trap and then dissociated and
ionized by electron collisions. The spectra were measured
for various electron beam currents ranging from $I_e = 1$ to 9
mA. Measurements were completed at nominal electron beam
energies of $E_e = 395$ and 475 eV. The space charge of the
electron beam at the trap for these measurements reduces the
electron beam energy seen by the ions by ≈ 20 eV below the
nominal values [23]. We use the space-charge corrected elec-
tron beam energies reported by [16], but we continue to refer
to the electron beam energy by their uncorrected energies.

Arthanayaka *et al.* [16] inferred the full width at half-
maximum (FWHM) of the radial extent of the electron beam,
Γ_e, from the EUV emission of the iron ions recorded using
a high-resolution grazing incidence spectrometer (HiGGS)
[24]. The EUV lines were from fast dipole-allowed transi-
tions, so that emission occurred only within the electron beam.
The observed iron lines were fit with Gaussian line profiles in
order to extract the intensities of the various lines of interest,
separate some line blends, and to quantify the linewidths.
The linewidths were essentially images of the electron beam.
The corresponding electron density, n_e, could then be inferred
based on the measured Γ_e and the known I_e and E_e.

The radius of the trapped ion cloud was measured using a
visible line emitted from a metastable level. As the lifetimes
of the metastable levels are long compared to the oscillation
period of the ions through the electron beam, the visible
light emission spans the entire ion cloud, giving an accurate
measurement of its dimensions. Specifically, we measured
the metastable Fe^{13+} $3s^2\,3p\,^2P_{3/2} - 3s^2\,3p\,^2P_{1/2}$ transition at
5302.9 Å [25]. This emission was isolated by using a 30-Å-
wide bandpass filter centered at 5320 Å. The lifetime of the
Fe^{13+} 5302.9 Å transition is 16.7 ms [26,27], which is much
longer than the ~ 0.01 μm transit time for ions to cross the
trap.

The ion cloud profiles were well fit using a sum of two
Gaussian components. The amplitudes A_1 and A_2 and the
FWHM Γ_1 and Γ_2 for the fits are provided by Tables 6 and
7 of Ref. [16]. In the following, we use these fits and other
relevant quantities from the experiment.

III. METHOD

To infer the ion energy distribution, we calculated ion orbit
trajectories and simulated the ion cloud. Each simulation be-
gins with a trial energy distribution for $\sim 10^4$ ions. As there are
no collisions in the simulation, the individual ion energies and
their energy distribution are conserved. Each ion is randomly
assigned an initial position and velocity drawn from the trial

energy distribution. Then the orbit trajectory for that ion is computed based on the forces from the radial electric field due to the electron beam and the axial 3 T magnetic field. After several orbits, sufficient time has passed to remove any correlations among the ion orbits from their initialization. We then construct a synthetic ion cloud measurement by projecting the ion positions onto one Cartesian axis. The synthetic and measured ion clouds are compared, and a least-squares minimization algorithm iteratively updates the trial energy distribution until the best-fit energy distribution is found.

A. Initialization of the ion energy distribution

The total energy of the ions is the sum of the kinetic energy and the electrostatic potential energy. In EBIT, electron-ion collisions transfer energy to the ions, and ion-ion collisions redistribute that energy among the ions. Physically, these collision processes determine the evolution of the ion energy distribution. However, our objective here is not to model the actual evolution of the ion distribution, but only to describe the ion energy distribution that produced our observed ion cloud. Thus, we assume that the ions have a fixed, albeit unknown, statistical distribution, and we ignore the collisions that explain how that distribution arose. Additionally, we neglect any collective motion of the ions.

Because collisions are neglected, energy is conserved along the ion trajectories, and the ion energy distribution, $f(E)$, is fixed by the initial conditions. For each ion, the total energy was set using a random number generator to draw an energy from an assumed energy distribution. We considered two approaches for specifying the energy distribution: we could directly set the form of the total energy distribution, or we could indirectly set the energy distribution by describing the initial position and velocity distributions. In principle, these are equivalent as they both set the initial ion energies, though in practice they allow the distribution to be varied in different ways. We worked with both approaches and obtained similar results. Here, we focus on those obtained using the direct method.

We described the initial energy distribution using a generalized energy distribution function of the form [28]

$$f(E) = \frac{x}{T^{3/2}} \frac{1}{\Gamma(3/2x)} (E - E_0)^{1/2} e^{-\left(\frac{E-E_0}{T}\right)^x}. \quad (1)$$

Here, E is the energy, T is an effective temperature, x is a parameter that controls the shape of the distribution, and Γ is the gamma function. With $x = 1$ this distribution has the form of a Maxwell-Boltzmann energy distribution and with $x = 2$ the form is that of a Druyvesteyn distribution [29]. We use this distribution because it is versatile, allowing for functions either sharper or broader than a Maxwell-Boltzmann distribution. Both x and T are free parameters in the ion cloud fits. The parameter E_0 is the zero of the energy distribution, which is the potential on the axis of the electron beam.

To calculate the trajectory of each ion, the initial positions and velocities are required, not just the total energy. Motivated by the physical consideration that the ions are formed by collisions with the electron beam, we set the initial radial distributions of the ions proportional to that of the electron beam density (see below). This sets the initial potential energy

for each ion. The remaining energy for each ion was then assigned to the kinetic energy, and the ions were given the corresponding initial velocity. This initial velocity vector was assigned to have a uniformly random orientation in the xy plane.

B. Ion trajectory calculations

We calculated the ion orbit trajectories for Fe^{13+} ions in EBIT-I in the two-dimensional plane perpendicular to the beam axis. This is justified by the axial symmetry of EBIT and the lack of any axial variation observed in the ion clouds measured by Arthanayaka *et al.* [16]. These ions are subject to an axial magnetic field of 3 T. They also experience a radial electric force from the electron beam. The electron beam density in EBIT-I is Gaussian, with

$$n_e(r) = n_0 e^{-r^2/2\sigma_e^2}, \quad (2)$$

where n_0 is the central density of the beam, σ_e is the Gaussian beam width, and the FWHM $\Gamma_e = 2.355\sigma_e$. These parameters can be derived from the quantities given in Tables 6 and 7 of Ref. [16]. There, the geometric average density $\bar{n}_e$ was reported, which corresponds to the density of the beam if it were a uniform cylinder of radius $r_e = 2\sigma_e$. The corresponding central density is $n_0 = 2\bar{n}_e$.

For this cylindrically symmetric Gaussian density distribution of the electrons, the radial electric field is given by

$$\mathcal{E}_{r,e}(r) = \frac{en_0\sigma_e^2}{\epsilon_0 r}(1 - e^{-r^2/2\sigma_e^2}), \quad (3)$$

where e is the unit charge and ϵ_0 is the vacuum permittivity. For computing the potential energy, one also needs to have the corresponding electric potential ϕ. Upon integrating Eq. (3), one obtains

$$\phi(r) = \frac{en_0\sigma_e^2}{\epsilon_0} \left\{ \ln \frac{r}{r_0} + \frac{1}{2}\left[E_1\left(\frac{r^2}{2\sigma_e^2}\right) - E_1\left(\frac{r_0^2}{2\sigma^2}\right) \right] \right\}. \quad (4)$$

Here E_1 represents the first exponential integral and r_0 is the radius at which the potential is defined to be zero. We have set $r_0 = 0.5$ cm, which corresponds to the inner radius of the drift tube in the trapping region. Note also that r_0 itself has no influence on the trajectories, as it is the electric field that determines the forces, and $\mathcal{E}_{r,e}(r)$ is independent of r_0.

Taking the limit of Eq. (4) for small r and multiplying by the ion charge q_i gives the potential energy of an ion on the axis of the electron beam:

$$E_0 = -q_i \frac{en_0\sigma_e^2}{\epsilon_0}\left[\frac{\gamma}{2} + \ln(r_0) + \frac{1}{2}\ln\left(\frac{1}{2\sigma_e^2}\right) + \frac{1}{2}E_1\left(\frac{r_0}{2\sigma_e^2}\right) \right]. \quad (5)$$

Here, γ is the Euler-Mascheroni constant with $\gamma \approx 0.577\,216$.

We also included the ion space charge. However, the ion space charge depends on the shape of the ion cloud. We defer the description of the electrostatic forces from the ions to Sec. III C.

The ion trajectories were calculated by integrating the equation of motion for the Lorentz force from the combined axial magnetic field and the radial electric field. The integration was carried out using the Boris algorithm [30,31]. We tested the orbits for energy conservation and found that
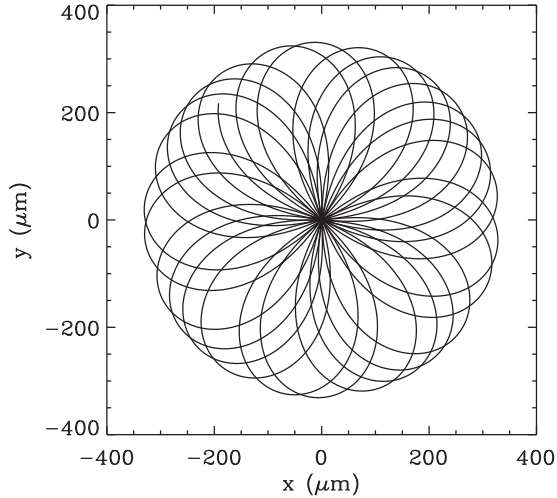
FIG. 1. Example of an ion orbit in EBIT-I.

energy is conserved to better than 2%. In many cases, the deviations from energy conservation are much less than 1%. The method is very fast, allowing for $\sim 10^4$ ion trajectories to be calculated in minutes. Figure 1 shows an example of an ion orbit trajectory. Note that the energy conservation is evident in the figure as the radial turning points of the orbits are constant.

Following the ions is necessary in order to remove bias from the initial position distributions. Setting the initial position and velocity distributions, $f(r, v)$, uses ad hoc assumptions that may differ from the $f(r, v)$ in the experiment. After several oscillation periods, the ion orbits become incoherent, removing the signatures of the initial $f(r, v)$, so that the orbits can be compared to the real ion cloud. After the ion orbits have become incoherent, the shape of the observed ion cloud no longer evolves (see also Appendix B of Ref. [16]). The typical radial oscillation period is about 0.01 μs. We sample the synthetic ion cloud after about 0.1 μs. Figure 2 illustrates the positions of 500 ion trajectories for the $I_e = 5$ mA and $E_e = 395$ eV experiment.
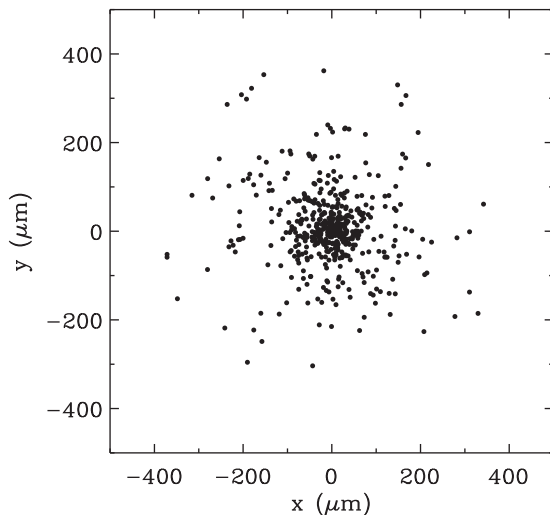

FIG. 2. Positions of 500 ions after a simulated 0.14 μs for the $I_e = 5$ mA and $E_e = 395$ eV case. The simulated ion cloud is obtained by making a histogram of the x-coordinates for all the ions.

C. Ion space charge

Given the final positions of the ions, we can compute the electric field and electric potential due to the ions. From the coordinates, (x, y), for the ions we make a histogram of the radial distribution of the ion cloud density, $f(r)$. Using Gauss's law, the radial electric field due to the ions is determined by numerically performing the integral,

$$\mathcal{E}_{r,i}(r) = \frac{Q_i}{\epsilon_0 r} \int_0^r f(r') r' \, dr', \tag{6}$$

where Q_i is the total number of ions per unit axial length in the trap. The electric potential is found by numerically integrating over the electric field.

The value of Q_i is very uncertain due to the unknown number of ions in the trap. It is very difficult to experimentally determine the number of trapped ions, and there have been few attempts to estimate it. Brown [32] studied Fe^{16+} and estimated that there were about 10^6 trapped ions in the EBIT for $I_e = 42$ mA and $E_e = 1150$ eV. If those ions are confined to the same volume as the electron beam, the positive charge density would be about half that of the negative charged electrons. Beiersdorfer *et al.* [33] and Schweikhard *et al.* [34] used ion cyclotron resonance mass spectrometry to estimate the number of $Kr^{33+} - -Kr^{36+}$ in EBIT, and they found that there were about 10^5 Kr ions at $I_e = 150$ mA and $E_e = 100$ keV. Porto *et al.* [21] assumed that the total ion charge was 65% of the electron charge. Based on these measurements, the trapped ion charge is typically roughly half that of the electrons, so we assume that the ion charge is 50% of the electron charge. This total ion charge is due not only to Fe^{13+}, but also to other charge states. Here, we assume that all ion space charge is distributed as it is for Fe^{13+}, which is the only ion whose spatial distribution is constrained by measurements.

To obtain a self-consistent ion cloud, we perform the calculation of the ion orbits iteratively. That is, the shape of the ion cloud determines the electric potential, which in turn modifies the shape of the ion cloud. For the initial run, we take $f(r)$ to be the one implied by the observed ion cloud. However, as described below, this initial ion cloud is probably different from the actual ion cloud in EBIT. After obtaining a model ion distribution, we recalculate $f(r)$ and repeat the process. A few iterations are sufficient so that subsequent ion clouds differ by 10% or less. The electric potential is not very sensitive to the exact shape of the ion cloud (see also Ref. [21]), and so this tolerance suffices.

D. Construction of a synthetic ion cloud

The trajectory calculation gives the Cartesian coordinates of a sample of ions. In the experiment, the ion cloud was measured using a visible light charge-coupled device (CCD). Thus, the experiment measured the projection of the ion cloud distribution onto one Cartesian axis, that is, the measured distribution is the Abel transform [35] of the ions' radial positions. Taking the x axis to be the plane of the CCD, we produce a synthetic image of the ion cloud by making a histogram of the x-coordinates of the ions. For the histogram, we use a bin size of 10 μm.

Figure 3 shows an example of our synthetic ion cloud compared to the empirical ion cloud for the $I_e = 7$ mA and
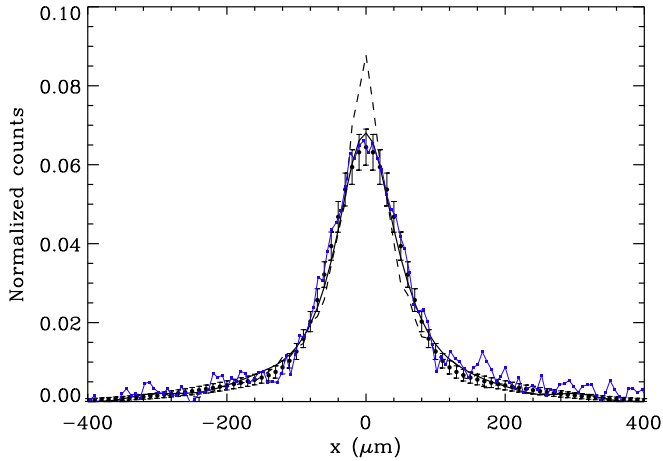
FIG. 3. Fit to the measured ion cloud for $I_e = 7$ mA and $E_e = 395$ eV. Solid connected square symbols in blue indicate the measured ion cloud, and the filled circles with error bars represent the double-Gaussian fit to those data and the associated counting statistical uncertainties. It is those smooth ion cloud data that the model attempts to replicate. The solid curve is the synthetic ion cloud obtained by fitting to the initial energy distribution $f(E)$ and then convolving with the estimated PSF for the optical system. The dashed curve illustrates the synthetic ion cloud before convolving with the PSF.

$E_e = 395$ eV case. The filled circles reproduce the function given by Table 6 of Arthanayaka *et al.* [16], which has been normalized by the total number of counts in order to compare with the synthetic cloud. That function is a fit to the data represented by the blue squares. The error bars represent counting statistical uncertainties on the measurement, based on the total counts reported in the experiment.

The inferred $f(E)$ for the 5 mA and 395 eV ion cloud is shown in Fig. 4. The best-fit parameters for this distribution as well as for other experimental conditions are discussed in detail in Sec. IV B.
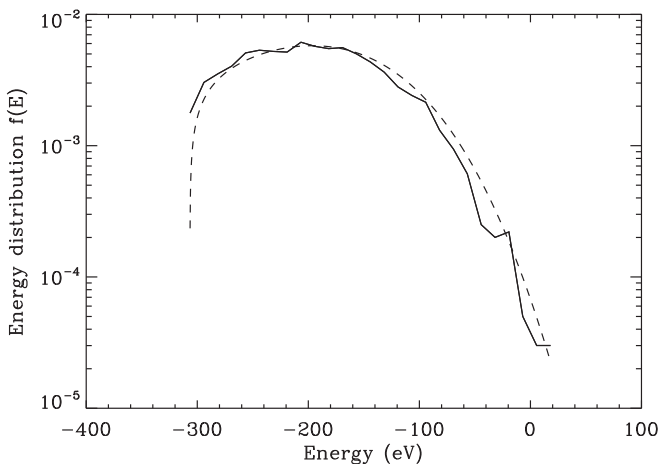

FIG. 4. Simulated $f(E)$ for the experiment with $E_e = 395$ eV and $I_e = 5$ mA. The solid curve is derived from the histogram of the ion energies in the model with 10^5 ions, and the "noise" in the curve is due to counting statistics. The dashed curve shows the analytical $f(E)$ distribution, from which the simulated ion energies are drawn.

We consistently find that our best-fit synthetic ion clouds have a taller and sharper peak than the measured ones. This occurs for different functional forms for $f(E)$ or $f(r, v)$, whether including or ignoring the ion space charge, and even for Maxwell-Boltzmann distribution ion clouds for which no numerical simulation is needed (discussed further in Sec. IV A). The most likely explanation for this consistent discrepancy is that diffraction and optical aberrations in the visible imaging system smooth out the actual ion cloud in the experiment. Such effects are present in every optical system, and consequently any measured ion cloud will be blurred compared to the ideal theoretical one.

We have estimated the point spread function (PSF) for the optical system that would be needed to account for the discrepancy between the observed and synthetic ion clouds. To do this, we convolved a Gaussian PSF with the synthetic ion cloud data and varied the width of the PSF to obtain the best least-squares fit to the measurements. For the 5 mA and 395 eV ion cloud, we find that the Gaussian width of the PSF would need to be roughly $\sigma \approx 21\ \mu$m.

For comparison, we can estimate the diffraction-limited resolution of the optical setup used in the experiment. The diffraction-limited angular resolution θ for a perfect circular lens of diameter d observing a wavelength λ is $\theta \approx 1.22\lambda/d$ [36]. Our system used a 4-in.-diam lens, however the lens was occulted down to 1 in. (2.54 cm) to reduce aberrations. This implies an angular resolution of 24.6 μrad for the observed wavelength of $\lambda = 5320$ Å. Since the beam is located 67 cm from the lens, we find that the diffraction-limited spatial resolution for a perfect optical system is about 16.5 μm. The optical system used in the experiment was known to have some optical aberrations, and so the larger inferred PSF width of $\approx 21\ \mu$m is reasonable.

To improve the correspondence between our synthetic ion cloud and the real measured one, we have convolved our model ion clouds with a PSF having $\sigma = 21\ \mu$m. Figure 3 illustrates the effect of the PSF convolution on the model ion cloud. In addition to correcting the sharp peak at $x = 0$, the smoothing also has numerical advantages. Since the ions are initialized stochastically, there are run-to-run fluctuations in the ions and in the resulting ion clouds. The PSF smoothes the model ion spatial distribution, effectively removing these fluctuations and thereby leading to a faster convergence of the chi-squared minimization.

IV. RESULTS AND DISCUSSION

A. Maxwell-Boltzmann distribution ion clouds

Before discussing ion clouds generated for an arbitrary ion energy distribution using the numerical model, it is useful to estimate some results using a Maxwell-Boltzmann distribution, i.e., applying the method of Porto *et al.* [21]. For a Maxwell-Boltzmann distribution, the radial spatial distribution of the ions is given by

$$f(r) \propto e^{-q_i \phi(r)/T_i}. \tag{7}$$

The observed image of the ion cloud is the projection of this cylindrically symmetric ion cloud onto an image plane. To compare this Maxwell-Boltzmann distribution ion cloud to the
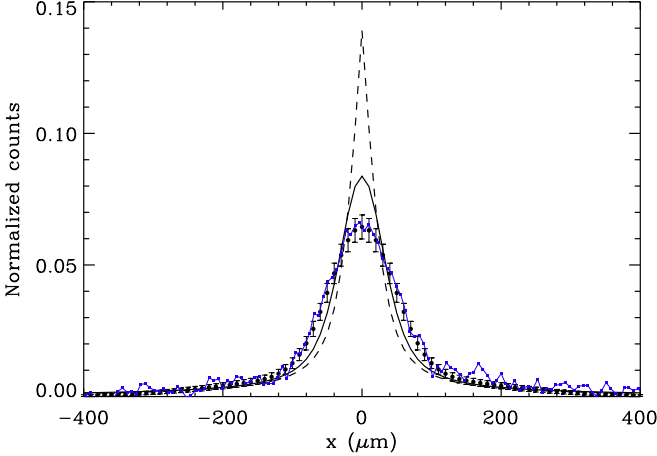
FIG. 5. Same as Fig. 3, but using a Maxwell-Boltzmann distribution. The solid curve is the Maxwell-Boltzmann distributed ion cloud after convolving with the estimated PSF for the optical system. The dashed curve illustrates the distribution before the convolution.

measured one, we find the Abel transform $F(x)$ of $f(r)$ [35],

$$F(x) = 2 \int_x^\infty \frac{f(r)r}{\sqrt{r^2 - x^2}} \, dy. \tag{8}$$

In this comparison, we normalize the theoretical and measured ion clouds so that $\int F(x) \, dx = 1$.

In Eq. (7), $\phi(r)$ is the electric potential due to both the electrons and the ions, the latter of which depends on $f(r)$. We used an iterative method to obtain a self-consistent $f(r)$ and $\phi(r)$. For the initial iteration, the ions are neglected and $\phi(r)$ is due only to the electrons. The resulting ion cloud is then used to recalculate $\phi(r)$ and generate an updated $\phi(r)$. The process is repeated until $f(r)$ converges. We considered the criteria for convergence to be that two subsequent iterations for $f(r)$ differ by not more than 2%.

In many cases, the Maxwell-Boltzmann distribution provides a reasonable approximation to the observed ion cloud (Fig. 5). In terms of the chi-squared value, χ^2, of the fits, the Maxwell-Boltzmann distribution has a χ^2 typically only a factor of a few greater than the trajectory calculation, although there are a couple of cases in which they are about equal, including the 7 mA case illustrated in Figs. 3 and 5.

Figure 6 compares the Maxwell-Boltzmann distributed ion cloud temperature to the radial electrostatic potential drop $\Delta\phi$ (see also Table I). It is clear that the best-fit ion temperature is very close to $\Delta\phi$, especially for smaller $\Delta\phi$, which corresponds to lower electron beam currents. This relation suggests that the ion energy distribution is limited by escape from the trap. If the ions had a higher temperature, the ions in the high-energy portion of the distribution would be lost, reducing the temperature.

B. Trajectory model ion cloud results

The trajectory calculation can produce synthetic ion clouds for any input ion energy distribution. As discussed above, we have used the generalized distribution function of Eq. (1) to characterize the ion energy distribution. Table II summarizes the results of that fit.
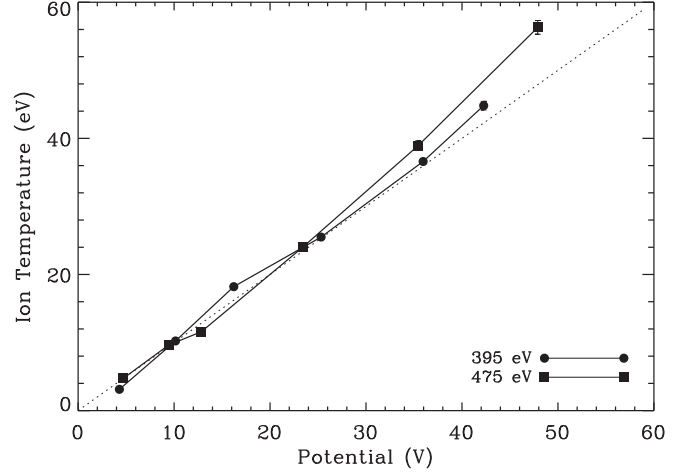

FIG. 6. Maxwell-Boltzmann distribution ion temperature T vs the radial electrostatic potential drop $\Delta\phi$ for the 395 eV (filled circles) and 475 eV (filled squares) electron beam energy. The dotted line indicates $T = \Delta\phi$.

The parameter x is related to the shape of the distribution, with $x = 1$ being a Maxwell-Boltzmann distribution and larger values of x corresponding to a sharper distribution with fewer particles at high energies. We find that the value of x increases with the beam current, or equivalently, with the radial potential difference. This implies that the ion energy distribution becomes increasingly nonthermal. Our method can diagnose the ion distribution, but it does not provide an explanation for it. Nevertheless, we can speculate. The main factors that influence the ion energy distribution are energy input from collisions with the electron beam, and energy losses from the escape of the most energetic ions. At low currents, energy input into the distribution may be low enough that inputs thermalize among the ions. At high currents, this balance may be lost with energy input causing rapid energization of ions that are then lost, leading to truncation of the tails of the distribution.

The second parameter of $f(E)$ is a temperature-like parameter, T. However, T is not directly related to the average energy of the ions, unlike the equilibrium temperature in a

TABLE I. Ion temperatures assuming a Maxwell-Boltzmann distribution.

E_e (eV)	I_e (mA)	$\Delta\phi$ (V)	T (eV)
395	1	4.3	3.13 ± 0.02
395	2	10.2	10.23 ± 0.14
395	3	16.2	18.21 ± 0.28
395	5	25.3	25.50 ± 0.38
395	7	36.0	36.60 ± 0.06
395	8	42.3	44.81 ± 0.63
475	1	4.7	4.75 ± 0.01
475	2	9.4	9.63 ± 0.02
475	3	12.8	11.59 ± 0.14
475	5	23.4	24.01 ± 0.36
475	7	35.4	38.94 ± 0.71
475	9	47.9	56.3 ± 1.0

TABLE II. Parameters describing $f(E)$.

E_e (eV)	I_e (mA)	$-E_0$ (eV)	T (eV)	x	$\langle E \rangle$ (eV)	$(r_{80,e}/r_{80,i})^2$
395	1	59.8	9.29 ± 0.48	1.00 ± 0.01	14.02 ± 0.54	0.23
395	2	126.4	68.2 ± 1.4	1.64 ± 0.09	57.2 ± 1.2	0.067
395	3	195.1	157.4 ± 3.5	2.81 ± 0.28	101.94 ± 0.58	0.047
395	5	316.7	192.3 ± 3.6	3.49 ± 0.61	118.7 ± 1.6	0.091
395	7	453.8	267.9 ± 6.5	3.78 ± 0.64	163.36 ± 0.26	0.081
395	8	521.7	321.2 ± 6.7	3.05 ± 0.51	203.8 ± 4.1	0.065
475	1	59.2	23.21 ± 0.64	1.06 ± 0.04	31.62 ± 0.98	0.078
475	2	118.3	83.6 ± 4.4	2.45 ± 0.48	56.5 ± 1.4	0.063
475	3	172.6	113.5 ± 2.0	3.29 ± 0.80	07.9 ± 2.7	0.090
475	5	295.0	195.9 ± 5.6	2.67 ± 0.46	128.8 ± 3.5	0.058
475	7	431.0	318.7 ± 9.6	3.46 ± 0.94	197.1 ± 5.2	0.040
475	9	557.7	436 ± 16	2.55 ± 0.33	291.0 ± 2.6	0.022

Maxwell-Boltzmann distribution. Instead we find the average ion energy for the generalized energy distribution by calculating the first moment of the inferred $f(E)$. For the energy distribution of Eq. (1), this is

$$\langle E \rangle = \int_0^\infty (E - E_0) f(E)\, dE. \qquad (9)$$

As E_0 is the minimum value of the energy distribution (i.e., in the absence of kinetic energy), we measure the average energy of the distribution above that value.

The ion energy increases in proportion to I_e, or equivalently to the beam density. Figure 7 shows $\langle E \rangle$ versus I_e for the two electron beam energies of 395 and 475 eV. There are several reasons that the average energy may increase with I_e or n_e. Increasing the electron density deepens the potential well, allowing higher-energy ions to be trapped. Hence, as I increases, so does the trap depth and the $\langle E \rangle$ of the trapped ions. This can be seen more directly in Fig. 8, which plots $\langle E \rangle$ against $-E_0$. As E_0 is negative and represents the zero of the energy distribution, $-E_0$ is positive and measures the

effective depth of the potential energy well in which the ions are trapped.

A higher electron current or density also increases the number of electron-ion collisions that transfer energy to the ions. Atoms arrive in the trap at room temperature. They are ionized and gain energy due to collisions with the electron beam. Therefore, more frequent collisions might also lead to a higher average ion energy.

Our measurements show that the ion energy depends strongly on I_e. For currents in the range of 1–9 mA, we find $\langle E \rangle \approx 10 - -300$ eV. From this we can derive an empirical relation $\langle E \rangle \approx 25 I_e$, where I_e is given in mA.

Figure 9 compares these average energies to the best-fit Maxwell-Boltzmann distribution temperatures. The average energy for a Maxwell-Boltzmann distribution is the temperature. To compare these quantities on the same basis, we have divided $\langle E \rangle$ by the ion charge, $q = 13$. Clearly, $\langle E \rangle$ and T are proportional to one another. This is expected since the ion energies are determined by the trap depth, regardless of the assumed shape of that distribution. The nonthermal distribution has an $\langle E \rangle$ that is less than half that of the T from the Maxwell-Boltzmann distribution $(\langle E \rangle / q)/T =$
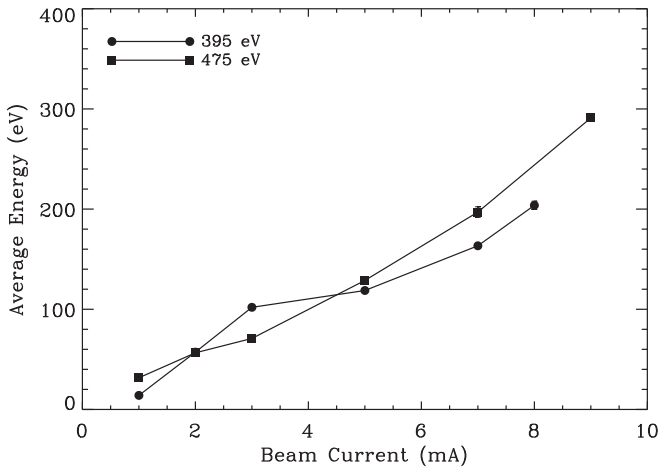

FIG. 7. The average energy of the ions $\langle E \rangle$ vs the electron beam current I_e. The filled circles show the results for the 395 eV electron beam energy, and the filled squares are for the 475 eV beam energy. The propagated uncertainties in $\langle E \rangle$ are shown, but are usually smaller than the symbol size.
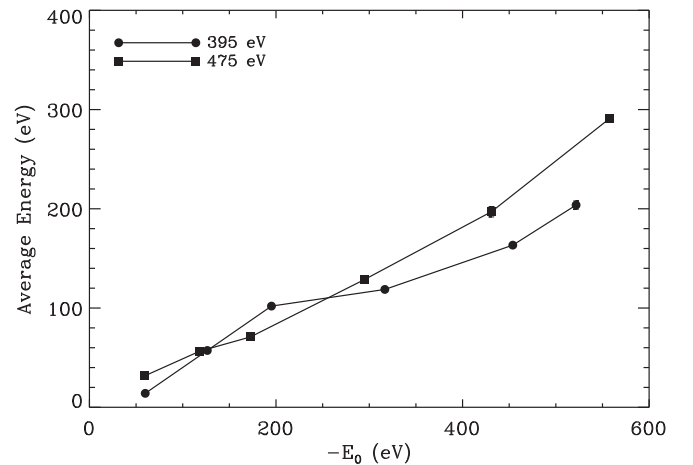

FIG. 8. Same as Fig. 7, except that here $\langle E \rangle$ is plotted as a function of $-E_0$, the magnitude of the minimum energy of the ion energy distribution.
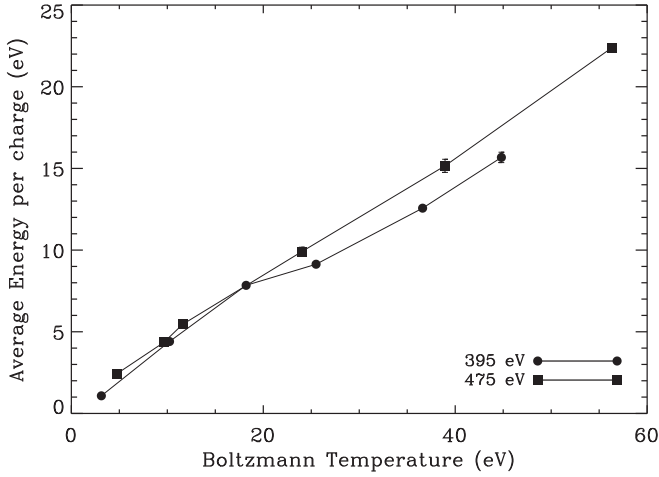
FIG. 9. The average energy of the ions per charge $\langle E \rangle / q$ vs the corresponding Maxwell-Boltzmann temperature T, for the 395 eV (filled circles) and 475 eV (filled squares) electron beam energies.

0.41 ± 0.05. This implies that the bulk of the ion distribution is trapped more strongly than would be expected for a Maxwell-Boltzmann distribution.

The most significant systematic uncertainties in our results come from the optical resolution of the imaging system and the estimate of the number of trapped ions. These could be resolved in future work by measuring the PSF of the optical system independently and by quantifying the number of trapped ions. Such data could then be readily incorporated into the methods presented here without fundamentally changing the procedure.

The PSF of the optical system smoothes the measured ion spatial distribution, especially by rounding off the sharp central peak in the modeled ion spatial distribution. In one test (for the 5 mA and 395 eV case neglecting ion space charge), we found that the best fit had a reduced chi-squared of $\chi_\nu^2 = 2.2$, but adding a PSF width of 21 μm improves the statistic to $\chi_\nu^2 = 0.77$. The effect is so large that other choices of the energy distribution may also produce reasonable fits. For example, we constructed an ion cloud from a uniform ion energy distribution that has the same average energy as the best fit for the generalized distribution, i.e., one that is constant from $E = 0$ to $E = 2 \langle E \rangle$. Without smoothing, this uniform distribution yields $\chi_\nu^2 = 4.4$, which is clearly worse than that of the generalized distribution. However, if the uniform distribution cloud is smoothed with the estimated PSF, then agreement is improved to $\chi_\nu^2 = 1.0$, which is a good fit. An optical system with better spatial resolution could increase the accuracy of the inferred $f(E)$.

The average energy $\langle E \rangle$ found by our fits is, however, robust to the ambiguity introduced by the optical system PSF. Distributions that have very different $\langle E \rangle$ from our results produce ion clouds that are significantly worse fits to the measurements. In addition, some aspects of the shape of the distribution are also robust; very different $f(E)$ distributions will lead to clear discrepancies with the measured ion cloud, even if $\langle E \rangle$ is kept the same as for the best fit. For example, a δ-function (beam) distribution with $f(E) = \delta(E - \langle E \rangle)$ pro-

duces a nearly uniform density ion cloud that clearly differs from the observed one.

Smoothing of the ion cloud peak by the PSF introduces a previously unappreciated systematic uncertainty into the electron-density-sensitive emission-line experiments. Arthanayaka *et al.* [16] sought to use the observed ion clouds to infer the effective average density, n_{eff}, that ions experienced along their orbits. Smoothing of the central peak makes it appear as though ions spend less time at the high densities near the center of the electron beam, and so Arthanayaka *et al.* underestimated n_{eff}. Using the trajectory calculations, we computed n_{eff} directly for the best-fit ion distributions, and we found that n_{eff} is about a factor of 1.4 greater than previously estimated.

The overlap of the ion cloud with the electron beam is another quantity that is commonly used to characterize the trapping in an EBIT, but we find that the sharper peak in the synthetic ion cloud only slightly changes this overlap factor compared to the measured ion cloud. It is conventional to consider the radius of the beam or cloud to be that radius that contains 80% of the particles, $r_{80,\mathrm{e}}$ or $r_{80,\mathrm{i}}$. Then the area overlap is given by $(r_{80,\mathrm{e}}/r_{80,\mathrm{i}})^2$. For the synthetic ion cloud, we find that the overlap factor is on average 0.08 ± 0.05 (see Table II). The $E_{\mathrm{e}} = 395$ eV and $I_{\mathrm{e}} = 1$ mA case appears to be an outlier, but in that case the experiment also showed a narrow ion cloud without the broader Gaussian component seen for the other conditions. These synthetic overlap factors can be compared to those expected from the measured ion cloud parameters given by Arthanayaka *et al.* [16], for which the overlap factor is about 0.05. The slightly larger overlap factor found using the modeled ion trajectories is probably due to the sharper peak in the center of the ion, but this difference is small and within the uncertainties.

A second source of systematic uncertainty is the number of trapped ions, which determines the magnitude of the ion space charge. The ion space charge reduces the radial electric field in the trap and the depth of the electric potential. As discussed above, we do not have a measurement of the number of ions. Rather, we have used a rough estimate based on other studies, finding that the trapped ion charge is about half that of the electron beam.

Our results allow us to predict qualitatively how a different ion space charge would affect the ion energies. In our measurements, $\langle E \rangle$ varies most strongly with the electrostatic trap depth. If we have estimated too few trapped ions, then we have overestimated the trap depth and our results for the magnitude of $\langle E \rangle$ are overstated. On the other hand, if we have estimated too many trapped ions, then the average ion energy is smaller than our estimate. This affects the magnitude of $\langle E \rangle$, but the trends with I_{e} and E_{e} should be unaffected.

In this work, we have neglected the role of axial trapping. Previous experiments have found that T_{i} increases with increasing axial trapping potential [19,20]. Our current measurements with varying radial potentials suggest that the reason for this dependence is that ions with sufficiently high energies escape so that a deeper potential well allows for higher energy ions to be trapped. It is necessary to apply the methods presented here to understand the characteristics of the ion cloud under typical EBIT conditions where axial

trapping and escape dominates with a lower trapping potential and a higher electron current.

V. SUMMARY

We have characterized the ion energy distribution $f(E)$ in an EBIT using a combined modeling and observational approach. Our diagnostic uses an ion trajectory calculation for a given set of experimental conditions and a trial $f(E)$ to construct a synthetic ion cloud. The form of $f(E)$ can accommodate nonthermal distributions. The parameters describing $f(E)$ are then varied until the synthetic ion cloud best matches the measurements. Here, we compared to the measurements of Arthanayaka *et al.* [16]. We find that the average ion energy, $\langle E \rangle$, increases with I_e and the depth of the radial potential. The inferred $\langle E \rangle$ ranges from about 10 eV to about 300 eV. We also compared to ion clouds from a thermal distribution, and we found that the ion temperature is approximately equal to the radial electrostatic potential drop across the trap. However, our more general results imply that the ion energy distribution is typically nonthermal with average ion energies less than half the temperature of the best-fit Maxwell-Boltzmann distribution. Our results suggest that the ion energy distribution is largely determined by the escape from the trap of ions that attain sufficient energy in the tails of the distribution.

The main sources of systematic uncertainty are the magnitude of the ion space charge and the spatial resolution of the optical system. The ion space charge reduces the depth of the potential well, which determines the $\langle E \rangle$ of the trapped ions. The spatial resolution constrains our ability to determine the details of $f(E)$, though $\langle E \rangle$ is expected to be robust to this uncertainty. The optical system PSF also smoothes out the central peak in the ion cloud. In the calculations we consistently find a sharp peak, which is not directly observed. If the actual ion spatial distribution is as strongly peaked as it is in the simulations, then the experimental effective densities were underestimated by ≈40%. Future work can improve these systematic uncertainties by quantifying the number of trapped ions and by reducing the PSF of the optical system.

[1] J. D. Gillaspy, Y. Aglitskiy, E. W. Bell, C. M. Brown, C. T. Chantler, R. D. Deslattes, U. Feldman, L. T. Hudson, J. M. Laming, E. S. Meyer, C. A. Morgan, A. I. Pikin, J. R. Roberts, L. P. Ratliff, F. G. Serpa, J. Sugar, and E. Takács, Overview of the electron beam ion trap program at nist, Phys. Scr., **T59**, 392 (1995).

[2] P. Beiersdorfer, Highly charged ion research at the livermore electron beam ion traps, Phys. Scr. **T120**, 40 (2005).

[3] M. A. Levine, R. E. Marrs, J. N. Bardsley, P. Beiersdorfer, C. L. Bennet, M. H. Chen, T. Cowan, D. Dietrich, J. R. Henderson, D. A. Knapp, A. Osterheld, B. M. Penetrante, M. B. Schneider, and J. H. Scofield, The use of an electron beam ion trap in the study of highly charged ions, Nucl. Instrum. Methods Phys. Res. B **43**, 431 (1989).

[4] D. A. Knapp, R. E. Marrs, S. R. Elliott, E. W. Magee, and R. Zasadzinksi, A high energy electron beam ion trap for production of high-charge high-Z ions, Nuc. Instrum. Methods Phys. Res. A **334**, 305 (1993).

[5] L. Gruber, J. P. Holder, J. Steiger, B. R. Beck, H. E. DeWitt, J. Glassman, J. W. McDonald, D. A. Church, and D. Schneider, Evidence for Highly Charged ion Coulomb Crystallization in Multicomponent Strongly Coupled Plasmas, Phys. Rev. Lett. **86**, 636 (2001).

[6] I. Draganić, J. R. Crespo López-Urrutia, R. DuBois, S. Fritzsche, V. M. Shabaev, R. S. Orts, I. I. Tupitsyn, Y. Zou, and J. Ullrich, High Precision Wavelength Measurements of Qed-Sensitive Forbidden Transitions in Highly Charged Argon Ions, Phys. Rev. Lett. **91**, 183001 (2003).

[7] C. Beilmann, J. R. Crespo López-Urrutia, P. H. Mokler, and J. Ullrich, High resolution resonant recombination measurements using evaporative cooling technique, J. Inst. **5**, C09002 (2010).

[8] L. Gruber, B. R. Beck, J. Steiger, D. Schneider, J. P. Holder, and D. A. Church, Highly charged ion trapping and cooling, in The Fifteenth International Conference on the Application of Accelerators in Research and Industry, AIP Conf. Ser. Vol. 475 (AIP, New York, 1999), pp. 56–61.

[9] R. E. Marrs and D. R. Slaughter, A high intensity electron beam ion trap for charge state boosting of radioactive ion beams, in The Fifteenth International Conference on the Application of Accelerators in Research and Industry, AIP Conf. Ser. Vol. 475 (AIP, New York, 1999), pp. 322–325.

[10] T. M. Baumann, A. Lapierre, S. Schwarz, K. Kittimanapun, and G. Bollen, Energy spread and time structure of ion beams extracted from the rea-ebit rare isotope charge breeder, *AIP Conf. Proc.* No. 1640 (AIP, New York, 2015), p. 80.

[11] M. A. Levine, R. E. Marrs, J. R. Henderson, D. A. Knapp, and M. B. Schneider, The electron beam ion trap: A new instrument for atomic physics measurements, Phys. Scr., **T22**, 157 (1988).

[12] M. B. Schneider, M. A. Levine, C. L. Bennet, J. R. Henderson, D. A. Knapp, and R. E. Marrs, Evaporative cooling of highly charged ions in EBIT: An experimental realization, *AIP Conf. Proc. No. 188* (AIP, New York, 1989), p. 158.

[13] G. Y. Liang, J. R. Crespo López-Urrutia, T. M. Baumann, S. W. Epp, A. Gonchar, A. Lapierre, P. H. Mokler, M. C. Simon, H. Tawara, V. Mäckel, K. Yao, G. Zhao, Y. Zou, and J. Ullrich, Experimental investigations of ion charge distributions, effective electron densities, and electron-ion cloud overlap in electron beam ion trap plasma using extreme-ultraviolet spectroscopy, Astrophys. J. **702**, 838 (2009).

[14] N. Nakamura, E. Watanabe, H. A. Sakaue, D. Kato, I. Murakami, N. Yamamoto, H. Hara, and T. Watanabe, Intensity

ratio of density-sensitive lines in Fe ions observed with a well-defined laboratory plasma, Astrophys. J. **739**, 17 (2011).

[15] E. Shimizu, A. Safdar, T. Tsuda, H. A. Sakaue, D. Kato, I. Murakami, H. Hara, T. Watanabe, and N. Nakamura, Measurements of density dependent intensity ratios of extreme ultraviolet lien emission from Fe X, XI, and XII, Astron. Astrophys. **601**, A111 (2017).

[16] T. Arthanayaka, P. Beiersdorfer, G. V. Brown, M. F. Gu, M. Hahn, N. Hell, T. Lockard, and D. W. Savin, Laboratory calibrations of Fe XII-XIV line-intensity ratios for electron density diagnostics, Astrophys. J. **890**, 77 (2020).

[17] P. Beiersdorfer, V. Decaux, S. R. Elliot, K. Widmann, and K. Wong, Temperature of the ions produced and trapped in an electron-beam ion trap, Rev. Sci. Instrum. **66**, 303 (1995).

[18] H. Adler, E. S. Meyer, F. G. Serpa, E. Takacs, J. D. Gillaspy, C. M. Brown, and U. Feldman, Fabry-Perot spectroscopy of a visible magnetic dipole transition in Ba^{34+}, Nucl. Instrum. Methods, Phys. Res. B **98**, 581 (1995).

[19] P. Beiersdorfer, A. L. Osterheld, V. Decaux, and K. Widmann, Observation of Lifetime-Limited X-Ray Linewidths in Cold Highly Charged Ions, Phys. Rev. Lett. **77**, 5353 (1996).

[20] P. Beiersdorfer, V. Decaux, and K. Widmann, Measurement of the temperature of cold highly charged ions produced in an electron beam ion trap, Nucl. Instrum. Methods, Phys. Res. B **98**, 566 (1995).

[21] J. V. Porto, I. Kink, and J. D. Gillaspy, Direct imaging of highly charged ions in an electron beam ion trap, Rev. Sci. Instrum. **71**, 3050 (2000).

[22] T. P. Arthanayaka, P. Beiersdorfer, G. V. Brown, M. Hahn, N. Hell, T. E. Lockard, and D. W. Savin, Measurements of the effective electron density in an electron beam ion trap using extreme ultraviolet spectra and optical imaging, Rev. Sci. Instrum. **89**, 10E119 (2018).

[23] D. Vogel, Report No. UCRL-ID-104990, Tech. Rep. (Lawrence Livermore National Laboratory, 1990).

[24] P. Beiersdorfer, E. W. Magee, G. V. Brown, N. Hell, E. Träbert, and K. Widmann, Extended-range grazing-incidence spectrometer for high-resolution extreme ultraviolet measurements on an electron beam ion trap, Rev. Sci. Instrum. **85**, 11E422 (2014).

[25] K. Schnorr, V. Mäckel, N. S. Oreshkina, S. Augustin, F. Brunner, Z. Harman, J. Ullrich, and J. R. Crespo López-Urrutia, Coronium in the laboratory: Measuring the Fe XIV green coronal line by laser spectroscopy, Astrophys. J. **776**, 121 (2013).

[26] P. Beiersdorfer, E. Träbert, and E. H. Pinnington, Astrophys. J. **587**, 836 (2003).

[27] G. Brenner, J. R. López-Urrutia, Z. Harman, P. H. Mokler, and J. Ullrich, Phsy. Rev. A **75**, 032504 (2007).

[28] S. F. Adams, J. A. Miles, and V. I. Demidov, Non-maxwellian electron energy distribution function in a pulsed plasma modeled with dual effective temperatures, Phys. Plasmas **24**, 053508 (2017).

[29] M. J. Druyvesteyn and F. M. Penning, The mechanism of electrical discharges in gases of low pressure, Rev. Mod. Phys. **12**, 87 (1940).

[30] C. K. Birdsall and A. B. Langdon, *Plasma Physics via Computer Simulation* (Taylor and Francis, New York, 2005).

[31] H. Qin, S. Zhang, J. Xiao, J. Liu, Y. Sun, and W. M. Tang, Why is Boris algorithm so good? Phys. Plasmas **20**, 084503 (2013).

[32] G. V. Brown, Spectroscopy of Fe L-shell line emission from Fe XVII- XXIV in the 10–18 A wavelength band, Ph.D. thesis, Auburn University (2000).

[33] P. Beiersdorfer, B. Beck, S. Elliot, R. Marrs, and L. Schweikhard, First fourier-transform ion cyclotron resonance signals of very highly charged atomic ions, Rapid Commun. Mass Spectrom. **8**, 141 (1994).

[34] L. Schweikhard, J. Ziegler, P. Beiersdorfer, B. Beck, S. Becker, and S. Elliott, Excitation and detection of icr modes for control and analysis of a multicomponent plasma, Rev. Sci. Instrum. **66**, 448 (1995).

[35] R. N. Bracewell, *The Fourier Transform and its Applications* (McGraw-Hill, New York, 1978).

[36] F. L. Pedrotti and L. S. Pedrotti, *Introduction to Optics*, 2nd ed. (Simon and Schuster, Englewood Cliffs, NJ, 1993).